

The Stellar Content of Obscured Galactic Giant HII Regions. VI: W51A

E. Figuerêdo¹

Department of Physics and Astronomy, The Open University, Milton Keynes, MK7 6AA, UK

E.Figueredo@open.ac.uk

R. D. Blum

National Optical Astronomy Observatory, 950 North Cherry Avenue, Tucson, Arizona, 85719

rblum@noao.edu

A. Damineli¹

IAG-USP, R. do Matão 1226, 05508-900, São Paulo, Brazil

damineli@astro.iag.usp.br

P. S. Conti

*JILA, University of Colorado
Campus Box 440, Boulder, CO, 80309*

pconti@jila.colorado.edu

and

C. L. Barbosa

*IP&D, Universidade do Vale do Paraíba, Av. Shihima Hifumi 2911, São José dos Campos
12244-000, SP, Brazil*

cassio@univap.br

ABSTRACT

We present K -band spectra of newly born OB stars in the obscured Galactic giant H II region W51A and $\approx 0.8''$ angular resolution images in the J , H and K_S -bands. Four objects have been spectroscopically classified as O-type stars. The mean spectroscopic parallax of the four stars gives a distance of 2.0 ± 0.3 kpc (error in the mean),

¹Visiting Astronomer, Cerro Tololo Inter-American Observatory, National Optical Astronomy Observatories, which is operated by Associated Universities for Research in Astronomy, Inc., under cooperative agreement with the National Science Foundation.

significantly smaller than the radio recombination line kinematic value of 5.5 kpc or the values derived from maser propermotion observations (6–8 kpc). The number of Lyman continuum photons from the contribution of all massive stars ($N_{\text{Lyc}} \approx 1.5 \times 10^{50} \text{ s}^{-1}$) is in good agreement with that inferred from radio recombination lines ($N_{\text{Lyc}} = 1.3 \times 10^{50} \text{ s}^{-1}$) after accounting for the smaller distance derived here.

We present analysis of archival high angular resolution images (NAOS CONICA at VLT and T-ReCS at Gemini) of the compact region W51 IRS2. The K_S -band images resolve the infrared source IRS 2 indicating that it is a very young compact HII region. Sources IRS2E was resolved into compact cluster (within 660 AU of projected distance) of 3 objects, but one of them is just bright extended emission. W51d1 and W51d2 were identified with compact clusters of 3 objects (maybe 4 in the case of W51d1) each one. Although IRS 2E is the brightest source in the K -band and at $12.6 \mu\text{m}$, it is not clearly associated with a radio continuum source. Our spectrum of IRS 2E shows, similar to previous work, strong emission in $\text{Br}\gamma$ and HeI , as well as three forbidden emission lines of FeIII and emission lines of molecular hydrogen (H_2) marking it as a massive young stellar object.

Subject headings: HII regions — infrared: stars — stars: early-type — stars: fundamental parameters — stars: formation

1. Introduction

The study of Giant HII regions (GHII – here taken to emit at least $10^{50} \text{ LyC photons s}^{-1}$, or $\approx 10 \times \text{Orion}$) in the near-infrared can address important astrophysical issues. The exploration of the stellar content of obscured Galactic GHII regions has been studied recently by several groups: Hanson et al. (1997), Blum et al. (1999, 2000, 2001), Figuerêdo et al. (2002, 2005), Okumura et al. (2000) and Bik et al. (2005, 2006). These observations revealed massive star clusters at the centers of the HII regions which had been previously discovered and studied only at much longer radio wavelengths.

The first step needed to trace the spiral structure of our Galaxy based on the spatial distribution of giant HII (GHII) regions is to derive spectroscopic parallaxes of OB stars in each embedded cluster. This is a well tested method in the optical window. We work in the near-infrared to overcome the obscuration at the optical wavelengths ($A_K/A_V \approx 0.1$) and use the recently developed spectral classification scheme in the near infrared (Hanson et al. 1996) to identify and classify the specific types of massive stars present. The uncertainty in the distance estimate is dominated by the scatter in the intrinsic M_V of O-type stars ($\pm 0.67 \text{ mag}$ - Vacca et al. 1996), leading to an uncertainty of 30% for a single O-type star. The uncertainty is diminished as spectra are accumulated, and can reach $<10\%$ if enough stars are observed. If B-type stars are included the individual accuracy is better as their M_K are more constrained given their longer main sequence

lifetimes.

Our procedure is independent of the traditional kinematic distance method based on radial velocity measurements of radio recombination lines and adoption of a Galactic rotation model. Almost all of the currently determined distances of Galactic GHII are based on this “kinematic” procedure which contains an ambiguity for directions inward of the solar circle and uncertainties introduced by random velocity components in the gas. In our previous work we were able to break the distance ambiguity of W31 (Blum et al. 2001), placing it on the near side of the GC at 3.4 ± 0.5 kpc from the Sun. In the case of W43 (Blum et al. 1999) and W42 (Blum et al. 2000) we also derived smaller distances than those inferred from the pure rotational model; in G333.1-0.4 (Figuerêdo et al. 2005), we also derive a smaller distance than given by the kinematic method (2.6 ± 0.4 kpc). Similar results have been found by other investigators using the same technique (Hanson et al. 1997; Bik 2004) for a number of other GHII. A recent H₂O maser study of the star forming HII region W3 finds a similar result based on maser parallax (Xu et al. 2006); i.e., W3 is closer than the kinematic distance and consistent with OB star absolute magnitudes in nearby associations lending credence to our results.

W51 is a complex of giant HII regions that was first detected by its free-free emission in the radio continuum (Westerhout 1958). The radio observations show that W51 is, in fact, composed of a group of individual sources spread in an area of one degree in the Galactic plane (Bieging 1975). The most luminous region in the W51 complex is G49.5-0.4 (R.A.= 19h23m42.02 and Dec. = +14d30m33.56s J2000), which is divided into eight smaller radio sources: W51A to W51H, ordered by R.A. W51A, one of the most luminous regions in the W51 complex, is located at a kinematic distance 5.5 kpc (near distance), adopting the value given by Russeil (2003) who used the 1985 IAU recommended values for the Sun to Galactic Center (GC) distance and rotation speed of the Milky Way, which are $R_0 = 8.5$ kpc and $\theta_0 = 220$ km s⁻¹. Although it is one of the most luminous star-forming regions in the Galaxy, this source is completely obscured in the optical wavelengths due to the large extinction at optical wavelengths along the line of sight.

Goldader & Wynn-Williams (1994) have imaged an area of $90'' \times 90''$ in the direction of W51A, using an angular resolution of $\approx 0.4''$ in the near infrared. In addition to the radio sources that had been previously discovered, IRS1 and IRS2, they identified a third bright source – IRS3. They also argued that IRS2 is in fact a small cluster with at least twelve point sources in *K*-band. They have compared the images from a narrow band filter, centered in *Br* γ , with *K*-band images, and they have concluded that the extended inter-cluster emission is thermal from ionized hydrogen and neutral helium. The surface brightness of the extended emission in the radio and near-infrared led to a extinction of $A_{K_S} = 2.6 \pm 0.3$ mag for W51A, with areas still more obscured. We used this work for the identification of candidates for spectroscopy in order to determine the distance of W51A by the spectroscopic parallax method.

Okumura et al. (2000) studied the properties of the stellar content of W51A in order to determine the stellar masses, ages, spatial distribution and IMF. They used *J*, *H* and *K* imaging on an

area of $15' \times 15'$ covering the G49.5-0.4 complex. These authors derived the interstellar extinction in the W51A direction by using the extinction in the visual band determined in a control field $20'$ from the source IRS2 along the Galactic plane. The histogram of the number of stars in each extinction bin shows two peaks at $A_V = 7$ and $A_V = 19$ mag. Okumura et al. (2000) explained this effect as the presence of the Sagittarius and Perseus spiral arms. By considering the distances of five kpc and 13 kpc for the two arms (Georgelin & Georgelin 1976), respectively, Okumura et al. (2000) derived an average interstellar differential extinction of 1.2 and 1.5 mag kpc $^{-1}$ in the visual band. Okumura et al. (2000) also found that the IMF slope in W51A agrees with the IMF slope in the control field in the range of masses between 10 and 30 M_\odot . On the other hand, they found an excess of stars more massive than 30 M_\odot .

In the present work, we are interested primarily in constraining the distance to W51A using spectroscopic parallaxes of newly born OB stars. In fact, with 8.71×10^{50} Lyman continuum photons per second (=NLyc – Conti & Crowther 2004), this would be equivalent to ≈ 20 O3V-type stars or ≈ 200 O7V-type stars (Martins et al. 2005). We present an investigation of the stellar content of W51A through JHK_S imaging and K -band spectroscopy (described in §2). In §3 we consider the photometry results, and in §4 we analyze the spectra. We determine the distance to W51A in §5 and discuss the results in §6.

2. Observations and Data Reduction

K -band ($\lambda \approx 2.2 \mu\text{m}$, $\Delta\lambda \approx 0.33 \mu\text{m}$) spectra of five objects in W51A were obtained on the nights of 2004 May 08 and 09 and 2004 June 01 using NIRI¹ on Gemini-North in queue-scheduled mode (GN-2004A-Q13). NIRI in $f/6$ mode delivers a plate scale of $0.12'' \text{ pix}^{-1}$. The $f/6$ camera and a four-pixel long slit ($0.48'' \times 110''$) were used. The K grism produces K -band spectra with a resolution of $R \approx 780$ for NIRI and the linear dispersion is $\lambda/\text{pix} \approx 7.08 \text{ \AA}/\text{pixel}$.

J ($\lambda \approx 1.25 \mu\text{m}$, $\Delta\lambda \approx 0.2 \mu\text{m}$), H ($\lambda \approx 1.64 \mu\text{m}$, $\Delta\lambda \approx 0.3 \mu\text{m}$) and K_S ($\lambda \approx 2.15 \mu\text{m}$, $\Delta\lambda \approx 0.3 \mu\text{m}$) images of W51A were obtained on the night of 2005 May 07 using the facility infrared camera ISPI² at the CTIO Blanco 4-m telescope (see Probst et al. (2003)). ISPI in F/6 mode delivers a plate scale of $0.3'' \text{ pix}^{-1}$ and a field of view of $10.25' \times 10.25'$.

All basic data reduction was accomplished using IRAF³. Each image was flat-fielded using dome flats and then sky subtracted using a median-combined image of independent sky frames obtained $10'$ North and $10'$ East from W51A for direct imaging and three dithered frames $1'-2'$

¹Gemini’s Near InfraRed Imager and spectrograph was built by the University of Hawaii’s Institute for Astronomy. See Hodapp et al (2003) for more details about the instrument.

²ISPI (Infrared Side Port Imager – “eye-spy”). More details about the instrument are available at the CTIO webpage.

³IRAF is distributed by the National Optical Astronomy Observatories.

far from the target for spectroscopy. One dimensional spectra were obtained by extracting and summing the flux in ± 4 pixel apertures. The extractions include local background subtraction from apertures $\approx 1''$ on either side of the object.

2.1. Photometry

The images of W51A were obtained in non-photometric (cirrus) conditions. Total exposure times were 15, 3.4 and 2.4 minutes at J , H and K_S , respectively. The individual J , H and K_S frames were shifted and combined. These combined frames have point sources with FWHM of $\approx 0.92''$, $0.91''$ and $0.78''$ at J , H and K_S , respectively.

Figure 1 shows a false color image, made by combining the three near infrared images and adopting the colors blue, green and red, for J , H , and K_S , respectively. This Figure shows two regions with strong $\text{Br}\gamma$ emission probably associated with embedded star clusters seen in the center (W51A – region 3 from Okumura et al. 2000) and in the NE of the image (region 2 from Okumura et al. 2000). The bluest stars are likely foreground objects, and the reddest stars are probably K_S -band excess emission objects, indicating the presence of hot dust associated with recently formed stars in the cluster. Background objects seen through a high column of interstellar dust would also appear red (but also fainter). The rectangle in Figure 1, indicates the region, including W51A, where DoPHOT (Schechter et al. 1993) photometry was performed on the combined images. DoPHOT detected a total of 2419 objects inside this rectangle in the K_S -band image. Of those 2419 objects, 1338 were also detected in H -band and 855 in all three filters. All objects detected in J or H -bands that were not picked up in K were excluded from our catalog because their errors were bigger than the cutoff limit (see below). Figure 2 shows a finding chart using the K_S -band image corresponding to the rectangular area of Figure 1. The numbers in the figure correspond to the brighter sources detected by DoPHOT.

Standard stars were not observed but flux calibration was accomplished using stars in the same field, available in the 2MASS⁴ All-Sky Point Source Catalog (PSC). Twenty uncrowded stars on the W51A images were used for this purpose. The DoPHOT magnitudes were compared to the 2MASS apparent magnitudes in order to define a zero point to the photometric calibration. The rms scatter in the zero point (difference between DoPHOT and 2MASS) in J , H , and K_S was 0.032, 0.051, and 0.082, respectively. The error in the mean for the twenty stars is then 0.007, 0.011, and 0.019 in J , H , and K_S , respectively. Uncertainties for the J , H and K_S magnitudes in W51A include the formal DoPHOT error added in quadrature to the error in the mean of the zero point offset. The sum in quadrature of both uncertainties results in typical bright star uncertainties of ± 0.019 , ± 0.028 and ± 0.038 mag in J , H and K_S , respectively. The derived magnitudes and

⁴2MASS: Two Micron All Sky Survey Skrutskie et al. (2006) - available at <http://www.ipac.caltech.edu/2mass/releases/allsky/>

colors of the stars labeled in Figure 2 are given in the Table 1.

The completeness of the DoPHOT detections was explored through artificial star experiments in the rectangular region of Figure 1 (see the discussion in Figueredo et al. 2005 for a description of the technique). The completeness is better than 90% for J and $H < 16.5$ and for $K_S < 16$. In other words, the detection of faint sources is more complete in J and H -bands than in K_S . This is likely because we are probably accessing mainly the (dense) foreground population and most of the fainter cluster members are not detected at this angular resolution (i.e., the true completeness limits in the *clustered regions of the image* are likely much brighter). The strong nebulosity will also hamper the detection of faint objects in the cluster region. Our primary goal in this paper is to derive the distance to W51A, and hence we only rely on the much brighter massive members of the cluster where crowding is not a significant factor. Indeed, the spectroscopic targets described below are in less crowded regions of W51A.

The mean of the differences between the input and output H and K_S magnitudes of the artificial stars experiment, considering only the range of magnitudes where the completeness is better than 90 %, are ≈ 0.07 and 0.11 , respectively. The results of this experiment are similar to the ones showed in Figueredo et al. (2005). The magnitudes errors determined by this method are much more realistic than the formal errors defined by DoPHOT. We adopted an arbitrary cutoff of 0.2 mag (stars with larger errors were excluded from further analysis).

2.2. Spectroscopy

In order to avoid spectral degradation by bad pixels, the total exposure time needed to obtain $S/N \sim 100$ was split and individual spectra were obtained at seven different positions along the slit. After each exposure, the telescope was offset by three arcsec along the slit. In two cases, two or three stars could fit in the same slit, therefore the exposure time was adjusted to the fainter star. We needed blank sky spectra in order to subtract the sky emission of each target spectrum that is contaminated by nebular emission. The sky background were obtained by median combination of three dithered exposures in a blank field one or two arcminutes from each target (total = 10 sky positions). Following this procedure, the K -band spectra of five of the brightest stars in the W51A cluster were obtained: RS6 (in this paper: #50 - see Figure 2), RS7 (#44) and IRS2East (IRS2E) from Goldader & Wynn-Williams (1994) and #2519 (#61) and #2670 (#57) from Okumura et al. (2000).

One dimensional spectra were obtained by extracting and summing the flux in \pm eight pixel apertures ($0.96''$) centered on the target in each dithered position. The extractions include local background subtraction from apertures $\approx 1''$ on either side of the object. Wavelength calibration was accomplished by using the spectrum of an Argon lamp obtained each night. The error of this calibration is $< 0.8 \text{ \AA}$ ($\sim 10\%$ of a pixel). In order to remove telluric features in the spectra of W51A stars, the A0V stars HIP92177 and HIP98640 were observed using an identical procedure, just after

or before those obtained for the target. At the time of the observation, both A0V stars have an air mass very close to the mean air mass attained by the targets in W51 during the observation period ($\Delta \approx 0.02$ airmass). The $\text{Br}\gamma$ photospheric feature was removed from the average A0V–type star spectrum by fitting and subtracting a Lorentz profile. Since the $\text{Br}\gamma$ region is relatively free from strong telluric features, this procedure is enough to obtain the template for telluric lines. The wavelength calibrated spectra were then divided by the continuum of the A0V–type star to remove telluric absorption.

The K –band classification scheme for OB stars is based on the (relatively weak) lines of CIV, HeI, NIII and HeII. The spectra of young stars in HII regions are often contaminated by the $2.058\ \mu\text{m}$ HeI and $\text{Br}\gamma$ nebular lines but these features are not used for classifying O–type stars (Hanson et al. 1996).

After the observations were obtained, it was found that Mader & Angione (1996) have identified the “A0V” telluric star HIP92177 (KOAql) as a binary system, and the secondary star is cooler than a G0–type star. Fortunately, the spectra of G–type stars don’t show any strong features near the most important lines used to identify the O–type stars that are located between $2.05\ \mu\text{m}$ and $2.2\ \mu\text{m}$. In fact, the Calcium, Iron and Sodium lines, together with the CO absorption bands, common in cool stars (Lançon & Rocca-Volmerange 1992), are located at wavelengths longer than $2.2\ \mu\text{m}$. In this work we thus consider the star HIP92177 as a telluric star, ignoring all lines longer than $2.2\ \mu\text{m}$ wavelength.

3. Results of the Photometry

The ISPI J , H and K_S –band images reveal W51A as an embedded star cluster readily seen in the center of Figure 2. Due to the strong nebosity it is hard to detect the faintest stars in this region. On the other hand, a comparison between the density of stars in the center of this figure with a sky image close to W51A, allow us to verify that the stellar density is higher in the center than the other areas of the image.

Okumura et al. (2000) found W51A is younger than 0.8 million years. This is in agreement with the photometric characteristics of this region, such as the high local reddening indicating that the massive stars have not completely shed their birth cocoons, and it is likely they are on the zero age main sequence (ZAMS). The cluster reddening can be approximated as $A_{K_S} \approx 1.7 \times (H - K_S)$ since the intrinsic colors of OB stars are nearly zero (Koornneef 1983); see Cardelli et al. (1989); Mathis (1990).

The $H - K_S$ versus K_S color magnitude diagram (CMD) is displayed in Figure 3. The labels in all plots refer to the same stars as in Figure 2. Both vertical lines indicate the position of the theoretical ZAMS shifted to 2.0 kpc (§6) and with interstellar reddening $A_{K_S} = 0.65\ mag$ (dashed line) and an additional “intra cluster” reddening component of $A_{K_S} = 3.27\ mag$ ($A_{K_S\text{total}} = 3.92\ mag$ – solid line). The strong nebosity in the cluster region, together with the crowding, can

explain the gap at $H - K_S \sim 2$ that appear in Figure 3 between $K = 13$ and $K = 15$ magnitudes. This gap is probably generated by the incompleteness as described in §2.1.

The $J - H$ versus $H - K_S$ color-color plot is displayed in Figure 4. In that diagram the solid lines, from top to bottom, indicate interstellar reddening for main sequence M-type (Frogel et al. 1978), O-type (Koornneef 1983) and T Tauri (Meyer et al. 1997) stars (dashed line). The solid vertical line between the main sequence M-type and O-type lines indicates the position of ZAMS. Asterisks indicate $A_{K_S} = 0, 1, 2$ and 3 extinction values (in magnitude). Dots are objects detected in all three filters. The error bars in both figures refer to the final errors in the magnitudes and colors. The small number of objects between both solid lines in Figure 4 means that most of stars have not been detected in the J -band images due the high extinction at this wavelength ($A_J \sim 10.5$ mag). Objects found to the right of the O-type star reddening line in the CMD of Figure 4, shown as a solid diagonal line, have colors deviating from pure interstellar reddening. This is frequently seen in young star clusters and is explained by hot dust in the immediate circumstellar environment.

For cases where the object has an apparent $J - H$ less than an unreddened O star, the explanation is not clear. Most of cases, but not all, those objects are faint stars. Such objects may actually be blends of two nearby stars of different colors which are inadvertently matched when merging the photometry from different filters. This can happen when a red cluster star is projected near to a bluer foreground star.

3.1. Reddening and Excess Emission

Two concentrations of objects are seen in the CMD around the two vertical lines. The first one appears around $H - K_S \approx 0.4$, which corresponds to an extinction of $A_{K_S} = 0.65$ mag ($A_V \approx 6.5$ mag) using the interstellar reddening curve of Mathis (1990). This concentration represents foreground stars (see also Figure 4). The foreground extinction can be estimated as $A_{K_S} \approx 0.3$ mag/kpc when using the distance of 2.0 kpc to W51A. Jonck-Sorensen & Knude (1994) found smaller values, $A_V \approx 1.8 - 2.5$ mag/kpc or $A_K \approx 0.18 - 0.25$ mag/kpc, for a field close to the galactic plane. On the other hand, Okumura et al. (2000) defined as foreground sources in the direction of W51A cluster, all objects with $A_K \leq 0.9$ mag/kpc. The second and smaller concentration of objects appears around $H - K_S \sim 2.0$ or $A_{K_S} = 3.27$ mag, indicating the average color of cluster members. A number of stars display much redder colors, especially brighter K -band sources. These objects are located at $H - K_S > 2.0$ and $A_{K_S} > 3.2$.

Determining the local reddening of a young cluster such as W51A is not simple, as the concentration of stars does not appear as a clear main sequence, and the scatter about the mean value of A_{K_S} is high. In fact, the differential “intra-cluster” reddening and the inclusion of very young sources produces the variation of the points on the CMD for $H - K_S > 0.4$. The local reddening can be determined through the colors of the O-type stars we have classified (see §4.1). The mean color

of the four stars spectroscopically observed are $(H - K_S) = 2.25$, which gives $A_{K_S} = 3.92 \text{ mag}$. The resulting local reddening in W51A direction, after subtracting the interstellar component, is then $A_{K_S} \approx 3.27 \text{ mag}$ ($A_V \approx 33 \text{ mag}$).

In order to place the ZAMS in the CMD, as Figure 3 shows, the reddening and the distance of W51A must be derived. The procedure used to transform bolometric magnitudes (M_{bol}) and effective temperatures (T_{eff}) into colors ($H - K$) and absolute K magnitudes has been given by Blum et al. (2000). No transformation has been derived between ISPI and the system used by Blum et al. (2000) (CIT/CTIO). The difference between both systems are negligible in comparison with the final uncertainties in the photometry. Figure 3 shows the ZAMS as a vertical dashed line, shifted to $D = 2.0 \text{ kpc}$ and reddened by $A_{K_S} = 0.65 \text{ mag}$ due to the interstellar component. When adding the average local reddening ($A_{K_S} = 3.27 \text{ mag}$), the ZAMS line is displaced to the right and downward, as showed by the solid line. A 5.5 kpc distance for W51A would move this ZAMS downward in the CMD by two magnitudes and the *observed* magnitudes for the spectroscopic targets would be inconsistent with a ZAMS luminosity class.

Besides the strong local reddening in the direction of W51A, the color-color diagram and CMD show several objects whose colors deviate from the pure interstellar reddening. These objects are located to the right of the O star reddening line in the CMD of Figure 3. We can estimate a lower limit to the excess emission in the K -band by supposing that the excesses at J and H are negligible, and that the intrinsic colors of the embedded stars correspond to normal OB stars. Indeed, we can follow the same procedure as Figuerêdo et al. (2002) by assuming that our sample of stars is composed of young objects (not contaminated by foreground or background stars) which have intrinsic colors in the range $(H - K)_0 = 0.0 \pm 0.06 \text{ mag}$ (Koornneef 1983). In Figuerêdo et al. (2005) we adopted for all objects the intrinsic colors of a B2 V star and from the difference between the observed $J - H$ and the adopted B2 V intrinsic $J - H$ color, we obtained the J -band extinction by using the adopted extinction law (Cardelli et al. 1989; Mathis 1990). The results for the same analysis in W51A are displayed in Figure 5.

In Figure 5 the solid line indicates $K_{exc} = 0$. Connected solid diamonds refer to the average value of the K excess in 1 magnitude bins. Dashed lines indicate 1, 2 and 3 σ from the average. Bright objects with very large excess (very positive values) in Figure 5 cannot be explained by errors in the dereddening procedure. The excess should be due to accretion disks and/or hot dusty envelopes around the less massive objects in the cluster. A few objects are well above the 3 σ scatter for otherwise normal stars in Figure 5.

As with in the case of G333.1-0.4, most of the stars in W51A (Figure 5) have a modest negative excess, about 0.2 magnitude. This negative excess has been explained by Figuerêdo et al. (2005) as a consequence of our assumption that all stars have the intrinsic color of a B2 V type star; in reality, most of the stars will have slightly positive intrinsic color. Our goal is to identify stars with a significant excess which would cause them to lie to the right of reddening line in Figure 4, so this modest negative excess for “normal” stars, or stars with a small excess is not important for

our purposes. In the following sections we have only corrected the K -excess for stars with positive excess as determined here, for all others we impose zero excess emission.

It is important to note that the excess emission as determined in this section is only a lower limit, since we assumed the excess was primarily in the K -band (but according to Figure 5, there are not many stars with large excess for the higher masses). Hillenbrand et al. (1992) have computed disk reprocessing models which show the excess in J and H can also be large for disks which reprocess the central star radiation. The K_S -band excess emission determined for IRS2E, about two magnitudes, is in agreement with the values found by Hillenbrand & Carpenter (2000) for young stars in the Orion cluster. Objects on the top of Figure 5 show excess emission still higher and it is an indication that probably such peculiar objects are, in fact, massive YSOs or ultra-compact HII (UHII) regions, as should be the case of IRS2E. Goldader & Wynn-Williams (1994) have found, besides IRS2, a pair of luminous sources in W51A - IRS1 and IRS3. The coordinates of IRS1 match those of #403 in figure 2, and IRS3 with #96 and #152, probably IRS3E and IRS3W respectively. Only #152 has been detected in H and K -band. Lower mass protostars also can show excess emission in K -band.

As we can see in Figures 3, 4 and 5, some objects in W51A are very bright, display very red colors and at the same time have excess emission well above the 3σ scatter for the average of normal stars. This is the case for objects such as IRS2W.

Given such evidence for circumstellar disks, we attempt to estimate by iteration the excess emission using Hillenbrand et al. (1992) models for reprocessing disks, such as was done in the case of G333.1-0.4 (Figuerêdo et al. 2005), to get a sense for how bigger the excess might be compared to that derived by assuming all the excess is in the K_S -band. This was done for the star we have detected in all three bands, IRS2W. The results corresponds to an excess emission of $K_{exc} = 3.58\ mag$ from a face-on reprocessing disk with a central source of $15\ M_{\odot}$ corresponding to the spectral type B0.5. The resultant reddening for this star was determined by using Mathis (1990) approximation as $A_{K_S} \approx 1.7 \times ((H - K_S) + 0.04 - 0.5)$. The resultant extinction for IRS2W, after correcting for the excess as determined above, is $A_{K_S} = 4.25\ mag$.

4. Results: Analysis of Spectra

The Gemini North/NIRI spectra of five objects in W51 sources are shown in Figures 6 and 7. All sources have been divided by a low-order fit to the continuum after correction for telluric absorption. The signal-to-noise ratio is $S/N \approx 100$. These spectra have been background subtracted with nearby ($\approx 1''.0$) apertures, though non-uniform extended emission could affect the resulting He I and Br γ absorption apparently present in the stars themselves.

In order to identify the spectral type of the stars we compared all spectra with the K -band spectroscopic standards presented by Hanson et al. (1996) and Bik et al. (2005). The features of greatest importance for classification are (vacuum wavelengths) the CIV triplet at $2.0705\ \mu\text{m}$,

2.0769 μm and 2.0842 μm (emission), the NIII complex at 2.116 μm (emission), and HeII at 2.1891 μm (absorption). Stars cooler than spectral type O7 show HeI (absorption) to the blue side of the NIII complex, at 2.1126 μm (which can be confused with nebular over-subtraction).

The NIII complex has been identified by Hanson et al. (1996) in early-O stars as being due to NIII(8–7). The fact that this transition is a multiplet system explains the broad profile of the feature, centered at 2.116 μm . It shows constant width through moderate variations in temperature and large variations in luminosity. The CIV triplet (2.071 μm , 2.077 μm and 2.084 μm) is typically weak and seen only in very high signal-to-noise spectra (Hanson et al. 1996). The present classification system laid out by Hanson et al. (1996) does not have strong luminosity-class indicators. Still, without nebular contamination (which is not the case presently), the HeI (2.0581 μm) and Br γ (2.1661 μm) features can be used to approximately distinguish between dwarfs plus giants on the one hand, and supergiants on the other (Hanson et al. 2005). Generally strong absorption in Br γ is expected for dwarfs and giant stars and weak absorption or emission for supergiants.

4.1. O-type Stars

Figure 6 shows four spectra that may be compared with the K -band spectroscopic standards presented by Hanson et al. (1996). The signal-to-noise ratio is $S/R \sim 100 - 120$, high enough to separate and identify the CIV triplet and NIII complex lines. The telluric absorption lines have been removed from the #44, #50 and #61 original spectra by using the HIP92177 spectrum. The spectrum of star #57 has been divided by HIP98640. The measured equivalent widths for the main lines for classification of the stars in Figure 6 are shown in the Table 2. The classification resulted in the spectral types indicated in the Figure.

The CIV triplet at 2.069–2.083 μm (emission) and the NIII complex at 2.116 μm (emission) identify the four sources in Figure 6 as early to mid O-type stars. The relatively strong NIII and HeII lines that appear in the spectrum of #57 indicate that this star is hotter than O6. On the other hand, the absence of CIV at 2.071 μm places #57 in the kO3–O4 subclass (Hanson et al. 1996). The CIV line appears very weak and blended with the third line of the triplet. The CIV line in the spectrum of the source #44 indicates that this star is cooler than a typical O4 and hotter than an O7-type star. The NIII line is still stronger than in the previous star, placing #44 in the kO5 subclass. In the spectrum of #50, the NIII line appears weaker than in #44 and for this reason this star is probably cooler than the previous one. The CIV triplet is still present, but weaker than in #44, placing #50 between the spectral type O6 and O7. The combination of features for source #61 suggest it is the coolest one in Figure 6, and we place it in the kO7–O8 subclass. As in our earlier work, we adopt a ZAMS classification due to the presence of massive YSOs in the cluster.

5. W51 IRS 2

5.1. High Resolution Images

W51 IRS 2 (hereafter IRS 2) consists of a number of a stellar objects surrounded by a peanut-shaped extended emission (as seen in low resolution images at $2.2\ \mu\text{m}$) of $\sim 15'' \times 15''$. Two bright sources were reported by Goldader & Wynn-Williams (1994) from low resolution near-infrared images: IRS 2E and IRS2 West (hereafter IRS 2W). IRS2 is also a radio source, named W51d (Martin 1972), however the radio peak does not coincide with the infrared peak (Genzel et al. 1982) IRS 2E.

In this section, we present high resolution images of IRS2 taken with the adaptive optics near infrared camera NAOS CONICA (NACO) (Lenzen et al. 2003; Rousset et al. 2003) at the ESO VLT UT4. The raw data were retrieved from the public database archive (ID 71C-0344(A)). We processed the data combining the dithered images and subtracting sky images taken with the same exposure time, but displaced from the target. The images were flat-fielded and a bad pixel map was applied to the final combined images. Photometry was performed by means of the IDL code XSTARFINDER (Diolaiti et al. 2000), a psf fitting algorithm suitable for adaptive optics assisted observations. The extracted fluxes were calibrated using the standard star P9150 (Persson et al. 1998) observed as part of the nighttime calibration set. The observing log of the images is presented in the Table 3. The zoomed box in Figure 1 is a false color image of IRS2, coded as red (K_s), green (H) and blue (J) and constitutes the highest resolution image obtained from this region until now (the H -band image was presented recently by Lacy et al. 2007).

The H and K images of IRS 2 are shown in the Figure 8. In both images, the circles represent the position of objects detected by Goldader & Wynn-Williams (1994) through a PSF fitting algorithm. The position of IRS2E is marked by a box and, as can be seen, three sources lie within it. Goldader & Wynn-Williams concluded that IRS2E is a small cluster of stars. The high resolution images suggest a somewhat different picture. Three sources are clearly identified both at H and K_S . Two of the sources (a and c) appear stellar, while the third (b) is an extended clump of emission. Furthermore, source c appears relatively blue and may be a foreground object. Source a is very red and the brightest K_S source in the IRS2 region. We thus associate IRS2E with a single unresolved source (a).

We present the IRS2 sources as open squares on the CMD in the Figure 3. We detected 36 sources in all three bands, however due to the low quality fitting of the two brightest sources in the J -band, they were removed. The source IRS2E, on the other hand is not detected in our J -band image.

5.2. Radio Sources and MIR Emission

IRS 2 hosts three UCHII regions (Gaume et al. 1993). The high resolution images show that a cluster of three objects can be associated with IRS2E within $1''$ (which would be 0.01 pc at a distance of 2.0 kpc). The main radio source W51d is a cometary UCHII region (Wood & Churchwell 1989), and the other two sources are W51d1 and d2 as showed in Figure 8. Goldader & Wynn-Williams (1994) noted that instead of extended emission, no NIR counterpart was found at the radio peak position, on the other hand, Okamoto et al. (2001) assumed that IRS 2W is the NIR counterpart of W51d, only by its proximity and by the visual inspection of the morphology of the extended MIR emission. Figure 9 is a composite image showing both radio and MIR emission overplotted on the K_S -band image of IRS2. The heavy black contour lines represent MIR emission at arbitrary units, from high resolution images taken recently at the Gemini South Observatory at $12.6 \mu\text{m}$ by us. A MIR study of W51A will be presented in a forthcoming paper (Barbosa et al. in preparation). The light white contour lines represent the radio emission, also at arbitrary units, taken from the radio catalogue of Wood & Churchwell (1989). Taking the K_S -band image as reference, we shifted the radio image on 0.8 arcsec to match the position of W51d and its NIR counterpart. This value is within the uncertainties of 1 arcsec as expected by UT4 pointing. The MIR image was shifted to match the MIR infrared peak of IRS2E and its NIR counterpart. The shift between MIR and NIR images amounts to 2 arcsec. The MIR images seem to have an uncertainty worst than the quoted 1 arcsec, specially at $25 \mu\text{m}$, so we can consider this shift value is within the uncertainties. The position of W51d₂ was derived from its relative position to W51d₁, comparing the coordinates presented by Wood & Churchwell (1989) and Gaume et al. (1993) for the former source.

The composite image shows IRS2W as the NIR counterpart of W51d, but also shows that IRS2W is not a MIR source. Okamoto et al. (2001), on the other hand identified IRS2W as the NIR counterpart of their MIR source OKYM3. The Western MIR emission peaks at the position of two stellar objects that are also coincident with the secondary peak of radio emission from W51d. This peak is spatially resolved in the MIR, however, and it is not clear if there is a buried source associated with it or if it is associated with an ionized cavity produced by IRS2W. We have recently obtained a Gemini NIFS spectrum of IRS2W which indicates it is indeed an O-type star of the hottest spectral type. This spectrum will be the subject of a forthcoming paper.

IRS2E is the brightest source in the K_S -band and at $12.3 \mu\text{m}$ as well, and it is not a radio source. This lack of emission at longer wavelengths may be due to its youth, it may be the case that this object has a low radio luminosity and/or a small emitting volume giving a low emission measure. However, it is worth noting that the radio maps presented by Gaume et al. (1993) show some extended emission *near*, but not coincident, with the position of IRS2E. Thus we conclude IRS2E is a massive young stellar object (MYSO), but we can not identify it as an UCHII. W51d₁ is seen as a radio, NIR, and MIR source and W51d₂ was not detected in the radio maps of Wood & Churchwell (1989) and may have weak MIR emission.

The high resolution images show that a cluster of three objects can be associated with IRS2E

within $1''$, which represents ~ 0.01 pc at the new distance of 2.0 kpc. It is also interesting to note that at the position of the radio source W51d₁ a small cluster of at least four sources is seen. A closer inspection of the images reveals two other sources, but they are too faint to be detected by a PSF fitting algorithm. We conclude that a small cluster of 4, maybe 6, sources (all of them within $0.3''$ or 660 AU) is the NIR counterpart of the radio source W51 d₁. A similar conclusion can be taken from the near infrared counterpart of source W51 d₂, since three sources are seen in its position, all of them separated by less than $0.3''$.

5.3. IRS2E Spectroscopy

The spectrum of the most luminous source in the K_S band in our sample, IRS 2E, is shown in Figure 7. The position of this source in Figure 3 shows that IRS 2E is more luminous in K_S than the O-type stars on the ZAMS which we classified in the previous section. OB stars can be very luminous in the NIR during their stage as a MYSO. This high luminosity is due to the excess emission in the K band (Figure 5). This K -band excess has to be accounted for if one wants to estimate the spectral type of the MYSO using its luminosity. The strongest emission lines are $\text{Br}\gamma$ ($\lambda = 2.166 \mu\text{m}$) and HeI ($2.058 \mu\text{m}$ and $2.113 \mu\text{m}$). Figure 7 shows a series of H_2 and $[\text{FeIII}]$ lines. Also, we confirm the detection of the “unidentified” infrared line at $2.288 \mu\text{m}$ reported by Okumura et al. (2001). This line was discussed earlier by Geballe et al. (1991) who did not detect it in IRS2 (apparently due to their large aperture of $5''$) but found it was common in planetary nebulae with middle excitation temperatures. Based on their observations, Geballe et al. (1991) were able to estimate the ionization potential of the species giving rise to the line which led Dinerstein (2001) to identify it with $[\text{Se IV}]$. The line is now known to be common in the spectra of planetary nebulae (PNe) (Sterling et al. 2007). A second line was identified by Dinerstein (2001) near $2.199 \mu\text{m}$ as being associated with $[\text{Kr III}]$. This line can be confused with an H_2 transition in lower resolution spectra. Our spectrum of IRS2E shows a line at this position and it is closer to the $[\text{Kr III}]$ position than the H_2 position. Independently of the present work, Blum & McGregor (2007) identified the $[\text{Se IV}]$ (and $[\text{Kr III}]$) line in two UCHII regions. Thus the “unidentified” line(s) appears more common than previously thought and may be produced in higher excitation regions very close to newly formed massive stars.

The spectrum of IRS 2E is very similar to the spectrum of the UCHII region G25.2-1.74 presented by Bik et al. (2005). Given the lack of a readily identifiable radio counterpart, this may simply reflect the nebular nature of IRS 2E and the environment within which it is found. Disentangling the internal and external excitation of IRS2E is beyond the scope of this paper.

6. The Distance to W51A

In the previous section we classified the spectra of five objects in W51A: four O-type stars and a MYSO. In this section, the distance to W51A is determined by using the spectroscopic and photometric results found for the four O-type stars. Table 4 summarizes the main properties of the O-type stars. We compute distances assuming the O-type stars shown in Figure 6 are zero-age main-sequence (D_{ZAMS} - column 5 of Table 4) or in the dwarf luminosity class (column 6). For the dwarf case, the distance is determined using the M_V given by Martins et al. (2005) and $V - K$ from Koornneef (1983). For the ZAMS case, we use the M_K from Blum et al. (2000) and adjust the M_K to account for the difference in M_V between the Vacca et al. (1996) and Martins et al. (2005) O star properties. Martins et al. (2005) have revised the dwarf O star M_V , and we have assumed the ZAMS M_V will be similarly shifted. For the spectral types considered here, the maximum change is to make the M_V 0.25 mag fainter.

The distance estimates are shown in Table 4. For the derived spectral types, we obtain distances of 2.0 ± 0.3 and 2.4 ± 0.4 kpc for the ZAMS and dwarf cases, respectively. The lack of luminosity class indicators do not allow us to unambiguously determine the distance, but the ZAMS value is preferred given the presence of massive YSOs in the cluster. The uncertainty quoted is the error in the mean.

An extra uncertainty on the derived distance comes from the interstellar extinction law. In this paper, we adopted the interstellar reddening curve of Mathis (1990). However, Messineo et al. (2005) and Nishiyama et al. (2006) predict $A_{K_S}/E_{H-K_S} \sim 1.5$ in contrast with the value 1.7 suggested by Mathis (1990). Higher values of interstellar extinction will result in an underestimate of the distance. The distances quoted above would be a factor of 1.28 larger for the extinction law predicting a smaller A_K .

6.1. The Lyman Continuum Flux

Conti & Crowther (2004) determined the number of Lyman continuum photons emitted per second by W51A as 8.71×10^{50} with the cluster located at a distance of 5.5 kpc. This corresponds to ≈ 20 O3V-type stars or ≈ 200 O7V stars (Martins et al. 2005). The new spectrophotometric distance we have determined by using four O-type stars is $D = 2.0 \pm 0.3$ kpc, considerably smaller than 5.5 kpc. The new distance brings the number of Lyman continuum photons down to $N_{LyC} = 1.15 \times 10^{50}$.

The Lyman continuum flux comes primarily from the four brightest stars which are well above our photometric completeness limit. We have calculated that the number of Lyman continuum photons from the contribution of all massive stars we have identified in the cluster is $N_{LyC} = 1.5 \times 10^{50}$ photons s^{-1} .

The observed N_{LyC} photons derived from radio techniques is only a lower limit to that emitted

by the stars, since some may be destroyed by dust grains or leaked through directions of low optical depth. On the other hand, due to the high extinction and crowding in the region some ionising stars may not have been detected in the J , H and K -bands. Therefore, both values found for the total $NLyC$ produced by the hot stars in W51A, by radio techniques and near-infrared, should be considered as lower limits. The $NLyC$ photons from the radio measurements and that derived from the star counts are in good agreement.

7. Discussion and Summary

We have presented J , H and K_S images of the HII region W51A obtained on the 4-m Blanco Telescope using the facility imager ISPI. The photometric results agree with the previous work, such as Okumura et al. (2000). K -band spectra of five of the brightest cluster members were obtained with Gemini North telescope using the instrument NIRI. Four of them have been classified as O-type stars and one as a massive young stellar object. We have derived the distance to W51A by using the spectroscopic parallaxes of four O-type stars. We also have presented archival images of the compact HII region IRS 2 taken with the adaptive optics camera NACO at the VLT. The high resolution images revealed a small cluster of four objects as the NIR counterpart of the UCHII region W51d₁ and another cluster with three objects at the position of the UCHII region W51d₂. The source IRS 2E was resolved into three sources and we identified the brightest source in the K band as IRS 2E. The K band spectrum of IRS 2E is very similar to that of an UCHII region, however, we do not explicitly classify it as so, because there is no distinct radio source with it.

The value we have derived for the distance to W51A by spectroscopic parallaxes of O-type stars, 2.0 ± 0.4 kpc, is considerably smaller than the kinematic distance: 5.5 kpc (Conti & Crowther 2004; Russeil 2003). The systematic uncertainties on the interstellar extinction law are not big enough to change this picture. As a consequence of this result, W51A is fainter than previously determined. Although the number of Lyman continuum photons is smaller with the new distance, $\sim 1.5 \times 10^{50}$ photons per second, W51A can still be classified as a giant HII region harboring a considerable number of massive stars.

The newly derived distance is much smaller than the distance (7 ± 1.5 kpc) derived from H₂O maser observations presented by Genzel et al. (1981, 1982) for the masers associated with W51A MAIN (about 1' south east of IRS2E) and the similar result (8.5 ± 2.5 kpc) for W51A NORTH derived by Schneps et al. (1981). The method used by Genzel et al. (1982) and Schneps et al. (1981) assumes the maser motions are random and isotropic. Imai et al. (2002) present somewhat more detailed models of the maser kinematics in W51A NORTH (centered within 1'' of IRS2E) and find that the motions are better explained by a radial out flow model which they use to fit the positions and outflow velocity. The distance derived from this technique is 6 ± 1.3 kpc, very close to the kinematic distance. On the other hand, they suggest the distance is completely covariant with the expansion velocity and the direction of the flow and the uncertainty permits a distance value of 7 kpc. Imai et al. (2002) further show that the masers for W51A MAIN and NORTH are

non-spherically symmetric and that there are significant residuals with respect to the assumption that all the maser spots emanate from a single point at the origin of the out flow (i.e. there are significant deviations for a simple radial out ward flow when looking at the derived maser space positions and velocity vectors). Using this assumption of random and isotropic motion for the water maser, Imai et al. (2002) estimated the distance of 4 kpc to W51A NORTH. This is in disagreement with the value found previously by Genzel et al. (1981). It is not clear what other models could fit the data or how serious the non-symmetry of the flow is in comparison to the model assumptions. In particular, it is not clear if a near distance model could fit the data.

The situation may be even more complex in light of recent mid infrared observations (in [Ne II]) made by Lacy et al. (2007). These investigators discovered a large “fan like jet” or outflow which is ionized as it enters the HII region (apparently from a source embedded in the molecular cloud) very close to W51A NORTH. They speculate that the ionized flow may have the same source as the W51A NORTH masers and this would require precession of the outflow since the ionized flow has a strong radial velocity while the masers are dominated by proper motions in the plane of the sky.

The masers of W51A NORTH are probably associated with IRS 2, while the O stars are somewhat further away in projection from IRS 2. The masers and O stars may trace different physical locations along the spiral arm and appear close only in projection. Within the uncertainty of the maser techniques, this explanation is less favorable since the distance derived for W51A MAIN is similar to the larger distance to W51A NORTH and W51A MAIN is closer (in projection) to several of the O stars (see Figure 2). If the O stars are actually unresolved multiple (massive) stars they would appear brighter and thus apparently closer. On average, this would require that nine stars of similar luminosity make up each object we have observed if we consider just the ratio of distances two kpc to six kpc. This seems an unlikely explanation. We are presently left with no satisfactory explanation for the distance discrepancy between the masers and radio observations on the one hand, and the near infrared spectrophotometric observations on the other.

The authors wish to thank Ed Churchwell for making available the radio map of W51 IRS2 in electronic form. We thank an anonymous referee for the careful reading of this paper and for the useful comments and suggestions which have resulted in a much improved version. AD and CLB are grateful to FAPESP and CNPq for support. PSC appreciates continuing support from the NSF. These results are based on observations obtained at the Gemini Observatory. The Gemini Observatory is operated by the Association of Universities for Research in Astronomy, Inc., under a cooperative agreement with the NSF on behalf of the Gemini partnership: the National Science Foundation (United States), the Science and Technology Facilities Council (United Kingdom), the National Research Council (Canada), CONICYT (Chile), the Australian Research Council (Australia), CNPq (Brazil), and CONICET (Argentina). This paper is partially based on observations made with ESO Telescopes at the Paranal Observatories under programme 71C-0344(A).

REFERENCES

- Bieging, J., 1975 in *H II regions and related topics*, Ed:T. L. Wilson & D. Downes, Vol.42, p.443
- Bik, A. 2004, PhD Thesis, Astronomical Institute Anton Pannekoek, the Netherlands
- Bik, A., Kaper, L., Hanson, M. M., Smits, M. 2005, *A&A*, 440, 121
- Bik, A., Kaper, L., Waters, L.B.F.M. 2006, *A&A*, 455, 561
- Blum, R. D., Damineli, A., Conti, P. S., *AJ* 1999, 117, 1392.
- Blum, R. D., Conti, P. S., Damineli, A., *AJ* 2000, 119, 1860.
- Blum, R. D., Damineli, A., Conti, P. S., *AJ* 2001, 121, 3149.
- Blum, R. D. & McGregor, P. J. 2007, to be submitted.
- Cardelli, J. A., Clayton, G. C., Mathis, J. S. 1989, *ApJ*, 345, 245
- Conti, P. S. & Crowther, P. A. 2004, *MNRAS*, 355, 899
- Diolaiti, E., Bendinelli, O., Bonaccini, D., Close, L., Currie, D., & Parmeggiani, G. 2000, *A&AS*, 147, 335
- Dinerstein, H. L. 2001, *ApJ*, 550, L223
- Figuerêdo, E., Blum, R. D., Damineli, A., Conti, P. S. 2002, *AJ*, 124, 2739
- Figuerêdo, E., Blum, R. D., Damineli, A., Conti, P. S. 2005, *AJ*, 129, 1523
- Frogel, J. A., Persson, S. E., Matthews, K., Aaronson, M. 1978, *ApJ*, 220, 75
- Gaume, R.A., Johnston, K.J., & Wilson, T.L. 1993, *ApJ*, 417, 645
- Geballe, T. R., Burton, M.G. & Isaacman, R. 1991, *MNRAS*, 253, 75
- Genzel, R., et al. 1981, *ApJ*, 247, 1039
- Genzel, R., Becklin, E.E., Wynn-Williams, C.G., Moran, J.M., Reid, M.J., Jaffe, D.T., & Downes, D. 1982, *ApJ*, 255, 527
- Georgelin, Y. M. & Georgelin, Y. P. 1976, *A&A*, 49, 57
- Goldader, J. D., & Wynn-Williams, C.G. 1994, *ApJ*, 433, 164
- Hanson, M. M., Conti, P. S., Rieke, M. J. 1996, *ApJS*, 107, 281
- Hanson, M. M., Howarth, I. D. , Conti, P. S. 1997, *ApJ*, 489, 698

- Hanson, M.M., Kudritzki, R.P., Kenworthy, M.A., Puls, J., & Tokunaga, A.T. 2005, *ApJS*, 161, 154
- Hillenbrand, L. A., Strom, S. E., Vrba, F. J., & Keene, J. 1992, *ApJ*, 397, 613
- Hillenbrand, L. A., Carpenter, J. M., 2000, *ApJ*, 540, 236
- Hodapp et al. 2003, "The Gemini Near-Infrared Imager", *PASP*, 115, 1388
- IAU - Comission 33: Structure and Dynamics of the Galactic System, 1985
- Imai, H., Watanabe, T., Omodaka, T., Nishio, M., Kameya, O., Miyaji, T., & Nakajima, J. 2002, *PASJ*, 54, 741
- Jonch-Sorensen, H. & Knude, J. 1994 *A&A*, 288, 139
- Koornneef, J. 1983, *A&A*, 128, 84
- Lacy, J. H., et al. 2007, *ApJ*, 658, L45
- Lançon, A. & Rocca-Volmerange, B., 1992, *A&A*, 96, 593
- Lenzen, R., Hartung, Markus et al. 2003, *SPIE*, 4841, 944
- Martin, A.H.M. 1972, *MNRAS*, 157, 31
- Mader, J. A., Angione, R. J. 1996, *PASP*, 108, 404
- Martins, F., Schaerer, D., & Hillier, D. J. 2005, *A&A*, 436, 1049
- Mathis, J. S. 1990, *ARA&A*, 28, 37
- Messineo, M., Habing, H.J., Menten, K.M., Omont, A., Sjouwerman, L.O., & Bertoldi, F. 2005, *A&A*, 435, 575
- Meyer, M. R., Calvet, N., Hillenbrand, L. A. 1997 *AJ*, 114, 288
- Nishiyama, S., et al. 2006, *ApJ*, 638, 839
- Okamoto, Y. K., Kataza, H., Yamashita, T., Takashi, M. & Onaka, T. 2001, *ApJ*, 553, 254
- Okumura, S., Mori, A., Nishihara, E., Watanabe, E. & Yamashita, T. 2000, *ApJ*, 543, 799
- Okumura, S., Mori, A. Watanabe, E., Nishihara, E., & Yamashita, T. 2001, *AJ*, 121, 2089
- Persson, S. E., Murphy, D. C., Krzeminski, W., & Roth, M., 1998, *AJ*, 116, 2475
- Probst, R. G., Montane, A., Warner, M., Boccas, M., Bonati, M., Galvez, R., Tighe, R., Ashe, M. C., van der Blik, N. S., Blum, R. D. 2003, *Proc. SPIE*, 4841, 411

- Rousset, G., Lacombe, F. et al. 2003, SPIE, 4839, 140
- Russeil D., 2003, A&A, 397, 133
- Schechter, P. L., Mateo, M. L., & Saha, A., 1993, PASP, 105, 1342
- Schneps, M. H., Moran, J. M., Genzel, R., Reid, M. J., Lane, A. P., & Downes, D. 1981, ApJ, 249, 124
- Skrutskie, M. F., et al. 2006, AJ, 131, 1163
- Sterling, N. C., Dinerstein, H. L., & Kallman, T. R. 2007, ApJS, 169, 37
- Vacca, W. D., Garmany, C. D., Shull, J. M. 1996, ApJ, 460, 914
- Westerhout, G. 1958, *Bulletin of the Astronomical Institute of the Netherlands*, Vol. 14, p. 215.
- Wood, D.O.S. & Churchwell, E. 1989, ApJS, 69, 831
- Xu, Y., Reid, M., Zheng, X., & Metnen, K. 2006, Science, 311, 54

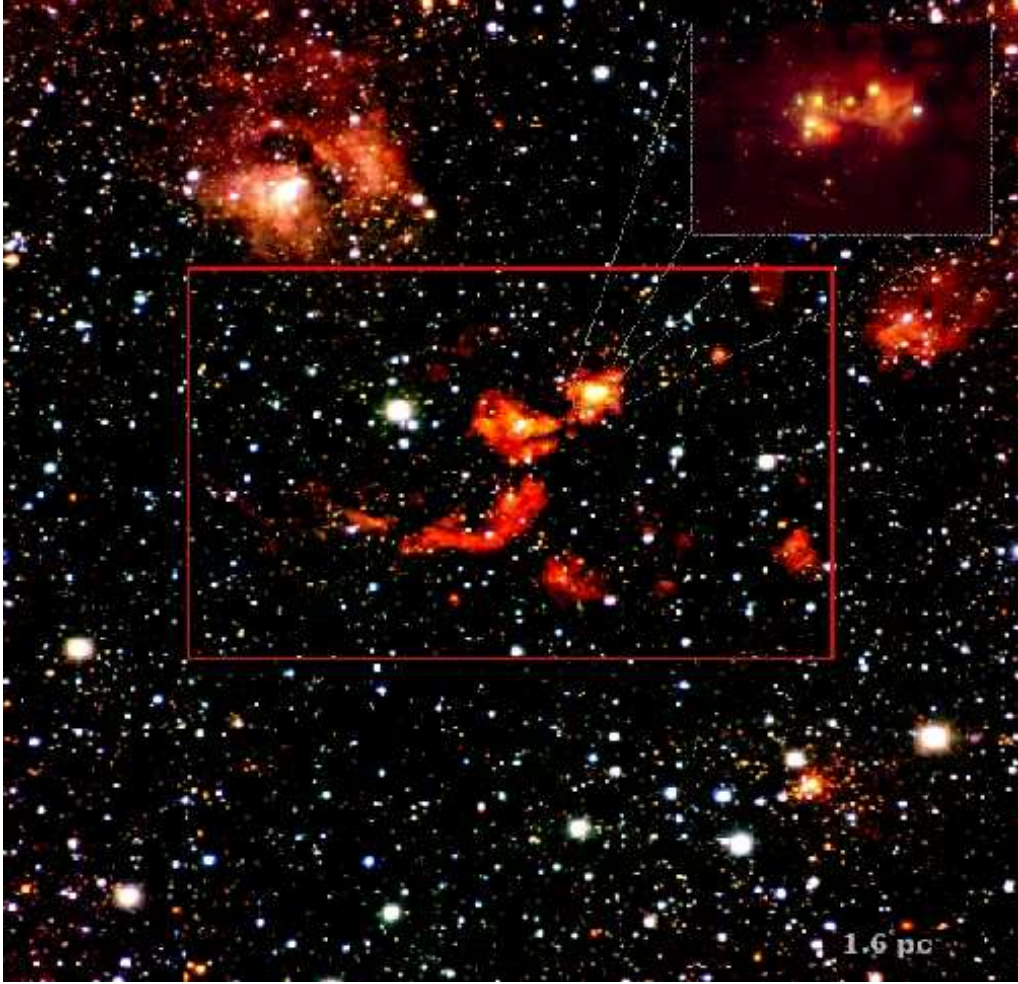


Fig. 1.— False color image of W51A: J is blue, H is green and K_S is red. The red rectangle indicates the region where DoPHOT photometry was performed. The coordinates of the center of the image are RA (2000) = 19h23m42.02s and Dec. = +14d30m33.56s and the size of the image is $10' \times 10'$ (plate scale = $0.3''/\text{pixel}$). North is up and East to the left. The zoomed box (top right) shows a VLT false color image of W51 IRS2 (see §5.1 and also Figures 8 and 9).

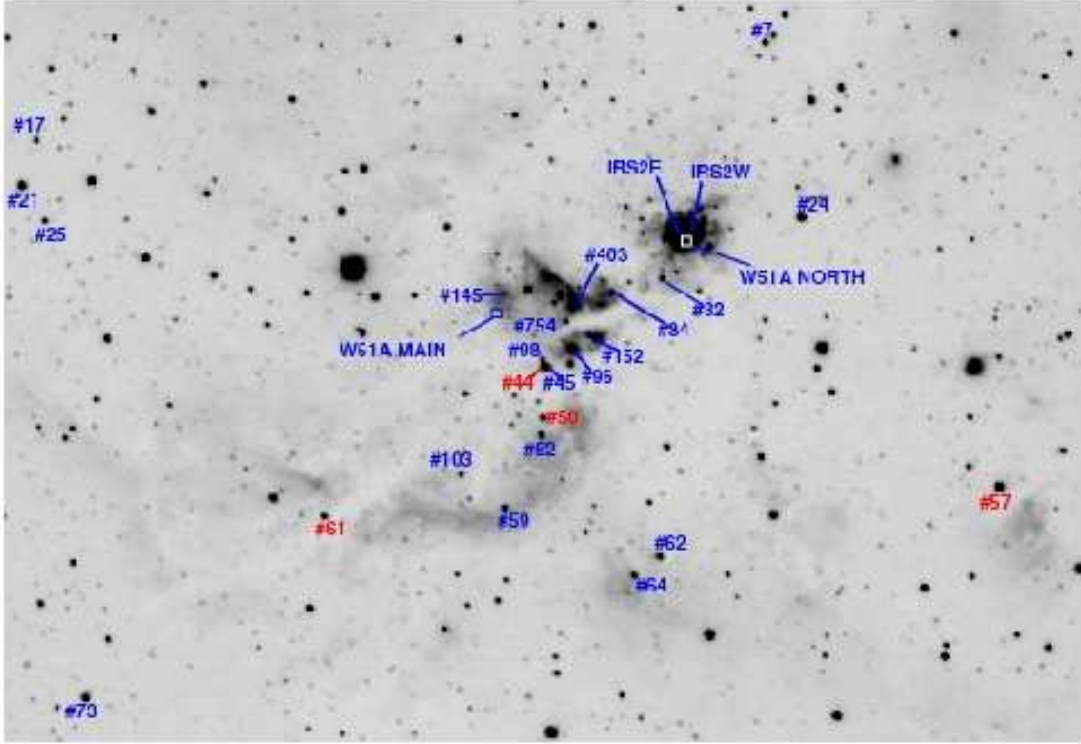


Fig. 2.— Finding chart using a K_S -band image of W51A, where DoPHOT photometry was performed (red rectangle in Figure 1). Object labels refer to the brightest cluster members detected by DoPHOT. *Squares* refer to the masers W51A NORTH and MAIN (see §7). stars #44, #50, #57 and #61 whose spectra show photospheric lines typical of O-type stars, have been used to determine the spectroscopic parallax of W51A. The size of the image corresponds to an area of $\approx 5.1' \times 3.5'$. North is up and East to the left.

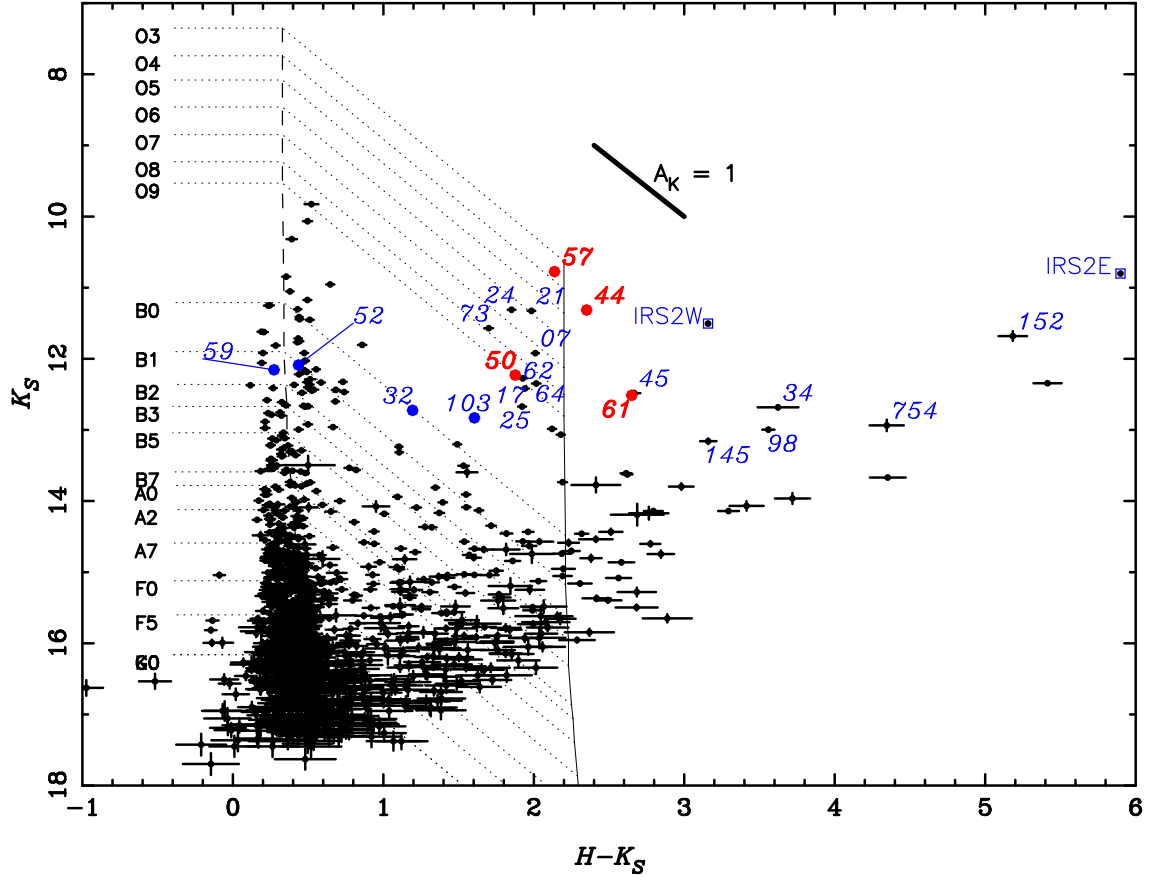


Fig. 3.— K_S vs $H - K_S$ color-magnitude diagram (CMD) of W51A showing the position of the theoretical ZAMS shifted to 2.0 kpc and with interstellar extinction $A_{K_S} = 0.65 \text{ mag}$ (dashed line). An additional “cluster” extinction component of $A_{K_S} = 3.27 \text{ mag}$ ($A_{K_S \text{ total}} = 3.92 \text{ mag}$) results in the ZAMS position indicated by the vertical *solid* line. Object number labels are the same as in Figure 2. *Open squares* indicate sources detected in IRS2 (see zoomed box in Figure 1 and §5.1 for more details).

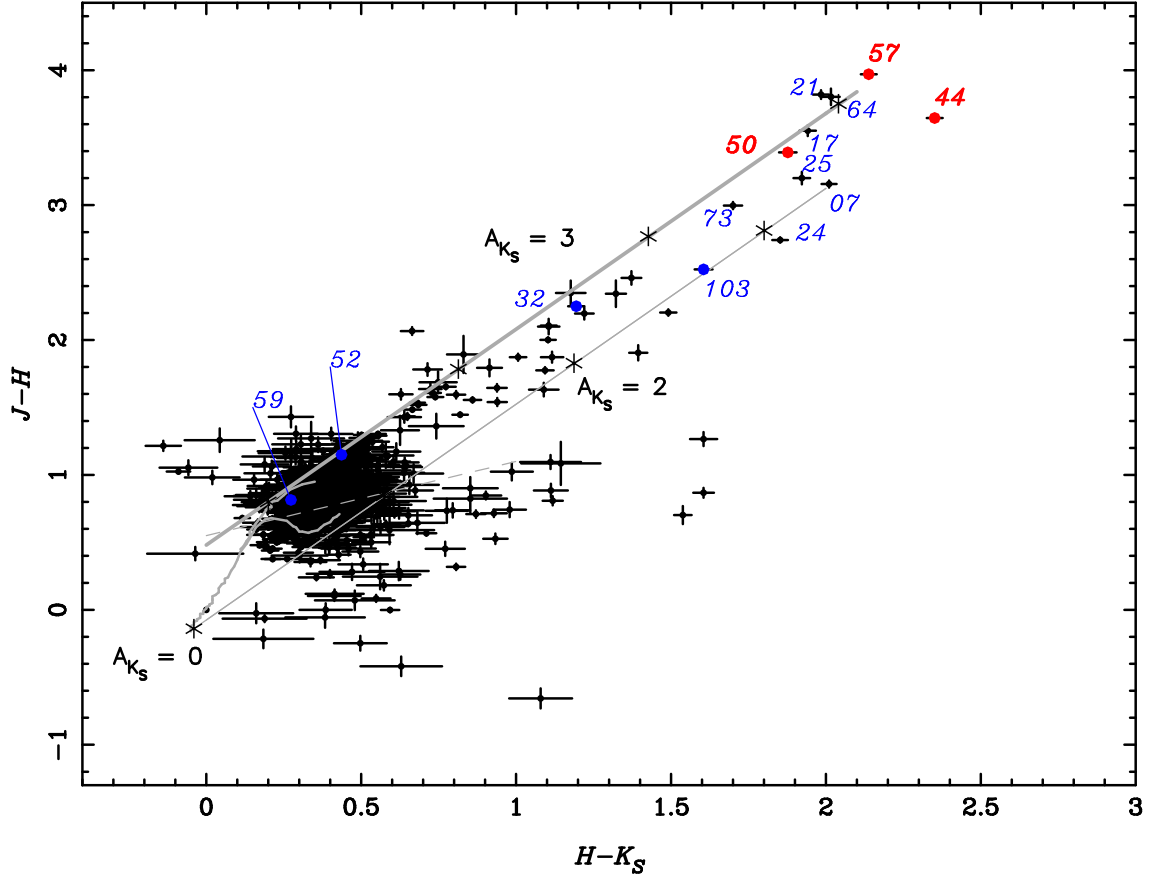


Fig. 4.— $J-H$ vs $H-K_S$ color-color plot showing the reddening line of M-type stars (*heavy solid line*), O-type stars (*solid line*) and T Tauri stars (*dashed line*). *Dots* refer to stars detected by DoPHOT in all three bands J , H and K_S . The *asterisks* indicate the corresponding A_{K_S} along the reddening vector. Object number labels are the same as in Figure 2 and 1.

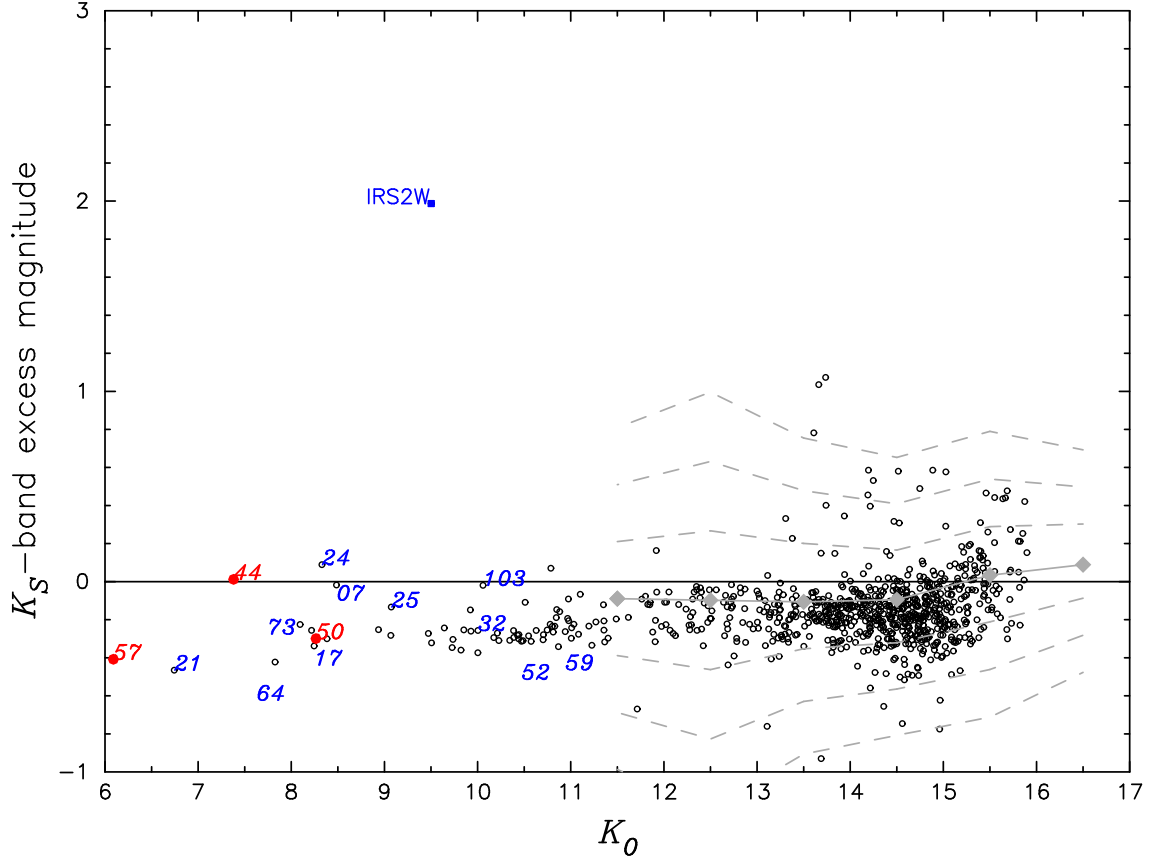


Fig. 5.— Excess emission as a function of dereddened K_S -band magnitude (K_0). Only objects detected in all three bands have been included. Circles indicate objects with measured J , H and K_S magnitudes. The solid line indicates $K_{exc} = 0$. Connected solid diamonds refer to the average value of the K_S excess in one magnitude bins. A 2 sigma clipping was applied to calculate the average values. Dashed lines indicate one, two, and three σ deviations from the average. IRS2W (Solid squares) have been detected in the VLT images (See §5.1 for more details). Very positive values represent circumstellar excess emission while small or slightly negative values do not; see text.

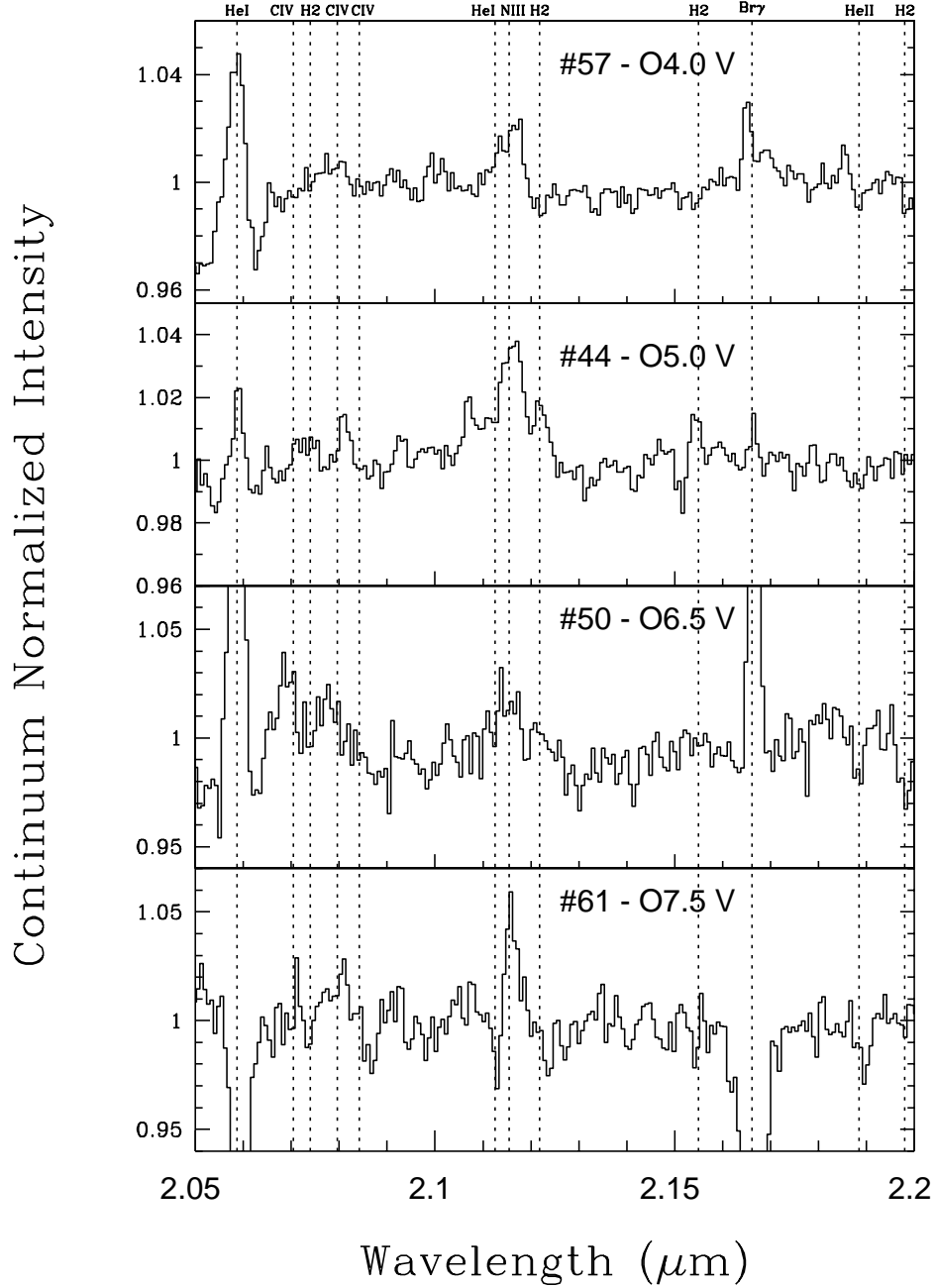


Fig. 6.— K -band spectra for the four brightest stars in the W51A: #57 (O4V), #44 (O5V), #50 (O6.5V) and #61 (O7.5V). The spectral type was determined by comparison with the O-type stars from Hanson et al. (1996). The spectral resolution of $R \approx 780$ gives a linear dispersion of $\approx 7.08 \text{ \AA/pixel}$. Spectra were summed in apertures $0''.96$ wide (eight pixels) by a slit width of $0''.48 \times 110''$ and include background subtraction from apertures centered $\leq 1''.0$ on either side of the object. Each spectrum has been normalized by a low-order fit to the continuum (after correction for telluric absorption). The spectra are often contaminated by the $2.058 \text{ }\mu\text{m}$ HeI and $\text{Br}\gamma$ nebular lines which can be over or under subtracted from the stellar source. The signal to noise ratio is $S/N \sim 100 - 120$.

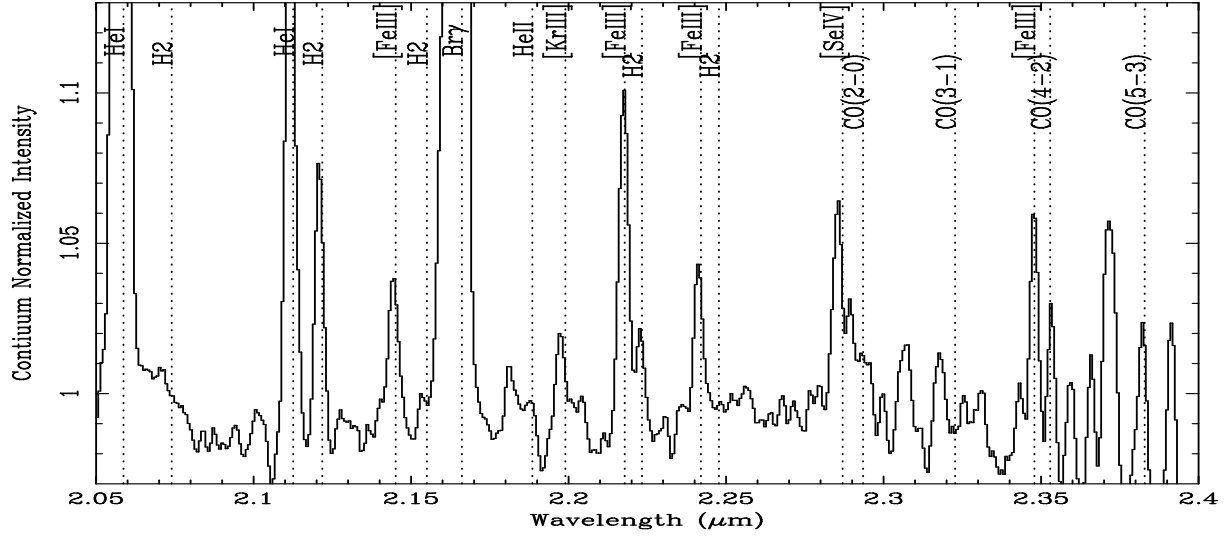


Fig. 7.— K -band spectrum of IRS2E taken with the same setup as the O-type star spectra shown in Figure 6.

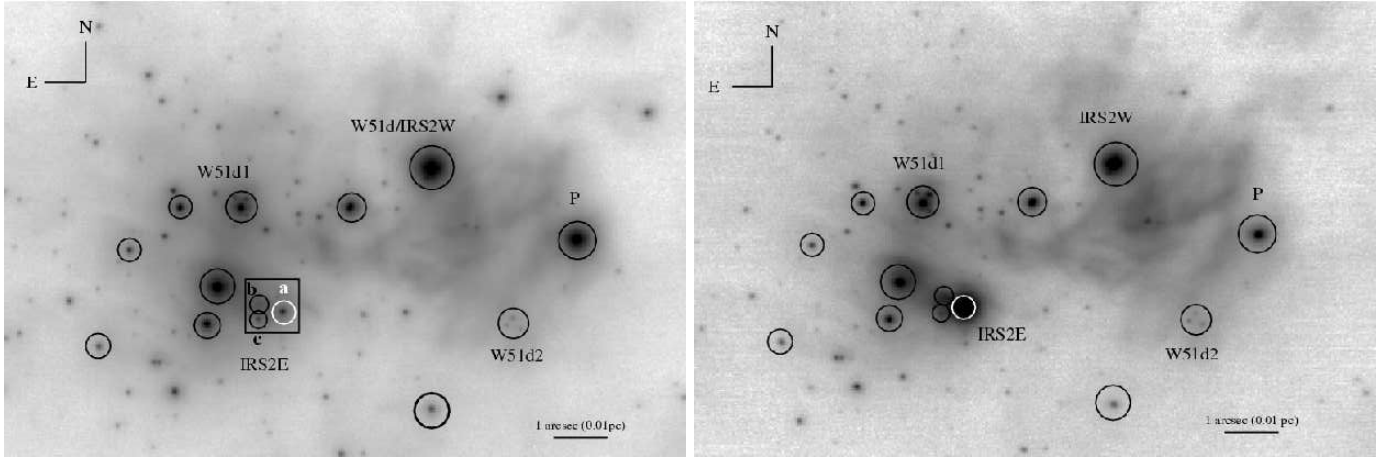


Fig. 8.— W51 IRS2 in the H -band (left panel) and K_S -band (right panel). The circles labeled a, b and c refer to the position of IRS2E, an extended emission (no stellar source) and a NIR source also detected by Goldader & Wynn-Williams (1994) respectively. The star labeled “P” is also detected on the POSS red plate. The position of IRS2E is marked by a box (sized $1'' \times 1''$). IRS2E is the brightest source in the field. The NIR counterparts of radio sources W51d, d₁ and d₂ are also indicated.

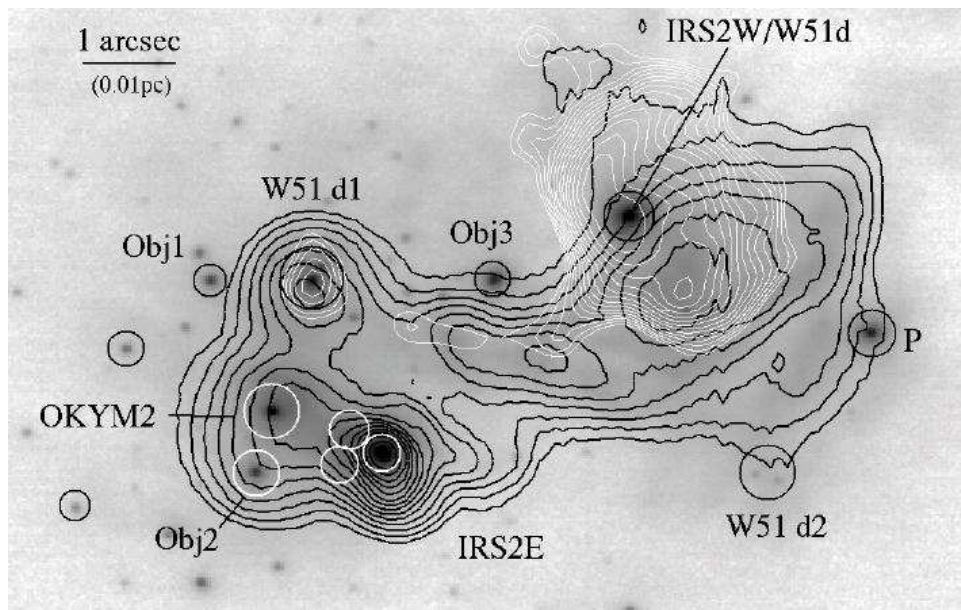


Fig. 9.— Composite image of IRS 2E. The K_S -band image is overplotted with radio emission contours from Wood & Churchwell (1989) in arbitrary units in light white contours from Wood & Churchwell (1989) and by MIR emission contours (C. Barbosa, unpublished), also at arbitrary units in heavy black contours. Sources are indicated by black or white circles to give the best contrast. W51d2 and the radio emission southern of W51d1 were not detected by Wood & Churchwell (1989), but fainter radio emission does extend toward IRS2E in the maps of Gaume et al. (1993).

Table 1. Colors and Magnitudes* Catalog

ID	J	H	K_S	$J - H$	$H - K_S$
IRS2E**	> 21	16.70 \pm 0.01	10.80 \pm 0.01	< 4.3	5.90 \pm 0.01
IRS2W**	16.47 \pm 0.01	14.66 \pm 0.01	11.50 \pm 0.01	1.81 \pm 0.01	3.16 \pm 0.01
#7	17.09 \pm 0.02	13.93 \pm 0.01	11.92 \pm 0.02	3.16	2.01
#17	17.91 \pm 0.04	14.36 \pm 0.02	12.42 \pm 0.02	3.55	1.94
#21	17.13 \pm 0.03	13.31 \pm 0.01	11.33 \pm 0.02	3.82	1.98
#24	15.90 \pm 0.01	13.16 \pm 0.01	11.31 \pm 0.02	2.74	1.85
#25	17.79 \pm 0.04	14.59 \pm 0.02	12.67 \pm 0.02	3.20	1.92
#32	16.17 \pm 0.01	13.92 \pm 0.01	12.73 \pm 0.02	2.25	1.19
#34	...	16.31 \pm 0.13	12.68 \pm 0.03	...	3.62
#44	17.31 \pm 0.01	13.67 \pm 0.01	11.31 \pm 0.02	3.65	2.35
#45	...	15.15 \pm 0.02	12.48 \pm 0.03	...	2.67
#50	17.50 \pm 0.02	14.11 \pm 0.02	12.23 \pm 0.02	3.39	1.88
#52	13.67 \pm 0.01	12.53 \pm 0.01	12.09 \pm 0.02	1.15	0.44
#57	16.88 \pm 0.02	12.91 \pm 0.01	10.77 \pm 0.02	3.97	2.14
#59	13.24 \pm 0.01	12.43 \pm 0.01	12.16 \pm 0.02	0.81	0.27
#61	...	15.16 \pm 0.02	12.51 \pm 0.02	...	2.65
#62	...	14.20 \pm 0.02	12.28 \pm 0.02	...	1.93
#64	18.17 \pm 0.06	14.36 \pm 0.02	12.35 \pm 0.02	3.80	2.02
#73	16.27 \pm 0.02	13.27 \pm 0.02	11.57 \pm 0.02	3.00	1.70
#98	...	16.56 \pm 0.03	13.00 \pm 0.02	...	3.56
#103	16.96 \pm 0.01	14.44 \pm 0.02	12.83 \pm 0.02	2.52	1.61
#145	...	16.32 \pm 0.04	13.16 \pm 0.04	...	3.16
#152	...	16.86 \pm 0.06	11.68 \pm 0.07	...	5.18
#754	...	17.28 \pm 0.08	12.94 \pm 0.08	...	4.35

*The sum in quadrature of the zero point uncertainty plus the PSF-fitting uncertainty define the final magnitude errors in J , H and K_S , see §2.

**VLT data

Table 2. Equivalent width (\AA) of strategic lines used to classify the O-type stars

Lines	#57	#44	#50	#61
HeI ($2.059\mu\text{m}$)	1.75 ± 0.13	1.42 ± 0.22	5.35 ± 0.37	$6.21 \pm 0.28^{*ab}$
CIV ($2.071\mu\text{m}$)	-	0.37 ± 0.05	$0.72 \pm 0.14^{*b}$	0.24 ± 0.12
CIV ($2.080\mu\text{m}$)	$0.32 \pm 0.04^{*b}$	0.96 ± 0.08	0.53 ± 0.14	0.61 ± 0.17
NIII ($2.116\mu\text{m}$)	0.95 ± 0.05	1.82 ± 0.09	$0.64 \pm 0.11^{*b}$	1.70 ± 0.21
Brg ($2.166\mu\text{m}$)	0.68 ± 0.09	0.41 ± 0.09	3.83 ± 0.22	$11.23 \pm 0.20^{*ab}$
HeII ($2.189\mu\text{m}$)	$0.21 \pm 0.10^{*ab}$	-	$0.51 \pm 0.16^{*ab}$	$0.63 \pm 0.12^{*ab}$

^{*b} – blended lines

^{*ab} – absorption lines

Table 3. NACO observations of W51 IRS2: instrumental set-up and observation logs. Camera S27 provides images with resolution of 27.15 mas/pixel and FOV of $28 \times 28 \text{ arcsec}$ employing an Aladdin InSb 1024×1024 pixel array.

Filter	Central Wavelength (μm)	Bandwidth (μm)	DIT ^a (s)	NDIT ^b (s)	PSF ^c (arcsec)	Date of observation	Seeing ^d (arcsec)
<i>J</i>	1.27	0.25	20	2	0.17	07/22/03	0.41
<i>H</i>	1.66	0.33	20	2	0.09	07/21/03	0.36
<i>K_s</i>	2.18	0.35	20	2	0.08	07/22/03	0.36

^aDIT corresponds to the exposure time of one image.

^bNDIT corresponds to the number of exposures.

^cPSF corresponds to the average PSF of detected objects in the field.

^dSeeing measured by the ESO Health Check Monitor at each band.

Table 4. Properties of O-type stars in W51A

ID	K_S	$H - K_S$	A_{K_S} ^a	D_{ZAMS} (kpc)	D_V (kpc)	Spectral Type
#44	11.31	2.35	4.08	1.7	2.0	O5
#50	12.23	1.88	3.28	2.8	3.6	O6.5
#57	10.77	2.14	3.72	1.9	2.1	O4
#61	12.51	2.65	4.59	1.4	2.0	O7.5
Average		2.25	3.92	2.0 ± 0.3 ^b	2.4 ± 0.4 ^b	

^a A_{K_S} was determined from $H - K_S$, using $(H - K_S)_0 = -0.05$ and the extinction law of Mathis (1990)

^bThe uncertainty quoted is the error in the mean.